

## BIOCHEMISTRY

# The role of DNA nanostructures in the catalytic properties of an allosterically regulated protease

Richard Kosinski<sup>1</sup>, Joel Mieres Perez<sup>2</sup>, Elisa-C. Schönweiß<sup>1</sup>, Yasser B. Ruiz-Blanco<sup>2</sup>, Irene Ponzio<sup>3</sup>, Kenny Bravo-Rodriguez<sup>2</sup>‡, Michael Erkelenz<sup>4</sup>, Sebastian Schlücker<sup>4</sup>, Guido Uhlenbrock<sup>3</sup>, Elsa Sanchez-Garcia<sup>2\*</sup>, Barbara Sacca<sup>1\*</sup>

DNA-scaffolded enzymes typically show altered kinetic properties; however, the mechanism behind this phenomenon is still poorly understood. We address this question using thrombin, a model of allosterically regulated serine proteases, engaged into DNA origami cavities with distinct structural and electrostatic features. We compare the hydrolysis of substrates that differ only in their net charge due to a terminal residue far from the cleavage site and presumably involved in the allosteric activation of thrombin. Our data show that the reaction rate is affected by DNA/substrate electrostatic interactions, proportionally to the degree of DNA/enzyme tethering. For substrates of opposite net charge, this leads to an inversion of the catalytic response of the DNA-scaffolded thrombin when compared to its freely diffusing counterpart. Hence, by altering the electrostatic environment nearby the engaged enzyme, DNA nanostructures interfere with charge-dependent mechanisms of enzyme-substrate recognition and may offer an alternative tool to regulate allosteric processes through spatial confinement.

## INTRODUCTION

Nucleic acids, and especially DNA, have often been used to isolate, reconstitute, and, in general, control protein activity to unravel nature's mechanisms and adapt them to our advantage (1–10). Among the variety of findings on DNA-enzyme systems, one common fact emerges: When an enzyme is tethered to a nucleic acid, the rate of the catalytic reaction changes. This phenomenon, initially observed almost 20 years ago (11) and further elaborated with the advance of DNA nanotechnology (12–28), still lacks a comprehensive explanation. Most of the reports on this topic highlight the increase in the catalytic efficiency of the enzyme upon its linkage to a DNA nanostructure. However, early studies on DNA-enzyme conjugates showed the opposite outcome, with reaction rates that decrease upon linking the enzyme to the DNA (13). In both cases, the extent of this change is affected not only by the sequence and length of the DNA strand but also by the type of enzyme and substrate under study (14), thus complicating the rationalization of the problem. Another point of relevance is that, so far, most of the progress in this matter relies on the use of enzyme cascades (typically glucose oxidase/horseradish peroxidase) scaffolded onto DNA nanostructures (22–28). Here, the components of the cascade are organized on top of a DNA surface with nanometer-scale precision, offering a tool to relate the enzymatic performance of the system to the intermolecular distance between its constituents. The increased reaction rates observed at shorter interenzyme spaces have been attributed to the occurrence of substrate channeling events (18, 19, 23–26). Other studies instead evidenced the importance of the electrostatic contribution given by the DNA surface to which the enzymes are scaffolded and proposed

alternative explanations that may apply especially when the rate of substrate diffusion is competitively high (27, 28).

The full picture is therefore still difficult to decipher, and several hypotheses have been advanced to explain the modified catalytic performance of DNA-tethered enzymes. These include the direct interaction of the DNA strand(s) with the enzyme and/or substrate (14, 21); the increased local concentration of the substrate in the vicinity of the protein active site, either as a consequence of favorable entropic contributions (15) or electrostatically driven steering (16); the establishment of a pH gradient (27, 28); or the creation of an ordered hydration layer at the DNA-protein interface (19, 21). All these hypotheses have been experimentally confirmed; nevertheless, the role of DNA on the enzymatic activity of a single DNA-tethered enzyme still remains partially undisclosed and even more arduous to generalize.

In the present study, we address this question using thrombin as a model enzyme. Thrombin is a monomeric serine protease of the chymotrypsin family that cleaves peptide substrates specifically after basic, mostly Arg, residues (29, 30). Two secondary anion-binding exosites, distant from the catalytic center, are required to add substrate specificity (31), and synthetic DNA aptamers have been developed that target these epitopes with nanomolar affinity (32–36). We use thrombin-binding aptamers (TBAs) to link thrombin to various DNA nanostructures. This approach has been already largely documented and provides the means to immobilize the enzyme to a target scaffold in a noncovalent fashion (37, 38). In this way, common issues of covalent DNA-protein conjugation can be bypassed, such as sample heterogeneity and permanent chemical modifications of the protein surface, which may result into unpredictable alterations of enzyme structure and function. Last, as our system is composed of a single enzyme molecule per DNA scaffold, distant-dependent parameters typical of multienzyme cascades become irrelevant, simplifying the analysis of the data and allowing to tackle the question of DNA-confined enzymatic catalysis at its core.

The special feature of thrombin is the multiplicity of its catalytic responses under slightly different conditions. This plasticity has been explained as the consequence of a highly regulated mechanism of

Copyright © 2022  
The Authors, some  
rights reserved;  
exclusive licensee  
American Association  
for the Advancement  
of Science. No claim to  
original U.S. Government  
Works. Distributed  
under a Creative  
Commons Attribution  
NonCommercial  
License 4.0 (CC BY-NC).

<sup>1</sup>Bionanotechnology, CENIDE and ZMB, University of Duisburg-Essen, 45117 Essen, Germany. <sup>2</sup>Computational Biochemistry, ZMB, University of Duisburg-Essen, 45117 Essen, Germany. <sup>3</sup>Dynamic Biosensors GmbH, 82152 Martinsried, Germany. <sup>4</sup>Physical Chemistry, CENIDE and ZMB, University of Duisburg-Essen, 45117 Essen, Germany.

\*Corresponding author. Email: barbara.sacca@uni-due.de (B.S.); elsa.sanchez-garcia@uni-due.de (E.S.-G.)

‡Present address: Max Planck Institute of Molecular Physiology, 44227 Dortmund, Germany.

allosteric activation, which relies on the communication between the catalytic pocket and mainly two regions on the protein surface, i.e., the sodium-binding loop and the exosite I (31, 39, 40). Subtle changes in the type and concentration of salts, pH of the buffer, and in the terminal residues of the peptide substrate that interact with the thrombin epitopes may result in more than 100-fold variation in the turnover number ( $k_{\text{cat}}$ ) and almost three orders of magnitude variation in  $K_M$  (41–43). The mechanistic details of these transformations have fostered decades of studies, earning this enzyme its deserved role of paradigm of allosterically regulated monomeric proteases (44). Being extremely sensitive to structural and charge-related factors, thrombin is therefore an ideal candidate to test both the scaffolding and the electrostatic role of DNA in ion-responsive enzymatic reactions, as those regulated by many serine proteases. These DNA-dependent effects may remain undisclosed in kinetically less compliant systems, and their deeper understanding is thus important in the effort to develop alternative tools for the modulation of enzyme activity.

Through the systematic investigation of the thrombin-catalyzed cleavage of different peptide substrates under various buffer conditions and DNA microenvironments, we here describe the complex role of DNA in the kinetics of an allosterically regulated monomeric protease. Our molecular dynamics (MD) simulations provide a structural rationalization of the experimental data and support our view of an active role of DNA in the mechanism of thrombin catalysis. Application of the transition state model allows to quantify the changes in the energy landscape of the reaction in different scenarios and provides the key to translate those changes into a variation of reaction velocity at different substrate concentrations. In our vision, DNA nanostructures are not merely passive scaffolds; rather, they actively participate to the catalytic cycle of the reaction by providing alternative kinetic routes for substrate hydrolysis. The final result is a network of catalytic reactions in which free and DNA-bound enzymes are kinetically coupled and DNA-driven fluxes increase proportionally to the DNA/enzyme binding affinity and the DNA/substrate electrostatic interactions. Kinetic simulations of a simplified version of our DNA-tethered systems support this hypothesis and suggest that DNA nanostructures act as modifiers of kinetic linkage schemes, the fine-tuning of which might be used to perturb the steady-state rate of an allosterically regulated enzyme, in a rational manner.

## RESULTS

### Design of the DNA-enzyme constructs

In all our samples,  $\alpha$ -human thrombin hydrolyzes a synthetic fluorogenic peptide substrate either in the absence or presence of aptamer ligands. The aptamers, when present, are either freely diffusing in solution or anchored to a DNA origami scaffold of defined shape (Fig. 1A). Hence, the entire system can be viewed as made of three elements: the enzyme, the substrate, and a DNA microenvironment, whose pairwise interactions must be considered to understand the complexity of the catalytic events taking place in the DNA-confined setting. The enzyme is the only constant term of the system, whereas the other two elements are modified in a systematic fashion to understand their individual and combined role in the kinetics of the reaction. We used three distinct peptide substrates of sequence FAM-GGfPR|SGGGK(BHQ-1)K-Aaa-OH (where f indicates a D-phenylalanine residue and Aaa is the variable amino acid; Fig. 1B).

All substrates carry a fluorescence resonance energy transfer (FRET) reporter pair [5-carboxyfluorescein/black hole quencher 1 (FAM/BHQ-1)], with the donor and quencher fluorophore located respectively at the P5 and P5' positions of the peptide. The thrombin-catalyzed hydrolysis of the substrate at the cleavage site (indicated by a vertical bar) results in the spatial separation of the dyes and loss of fluorescence quenching. The consequent increase in the fluorescence signal of the donor is then used for monitoring the progress of the reaction during time. The three substrates differ only in the C-terminal amino acid (Aaa): Here, the presence of a Gly, Asp, or Lys residue results, respectively, in a neutral (0), negative (–1), or positive (+1) net charge of the substrate at pH 7. Correspondingly, the three substrates are indicated as S(0), S(–1), and S(+1).

The other variable of the system is the DNA microenvironment. This has been systematically changed to assess the effect of diverse structural and electrostatic factors on the catalytic performance of the enzyme/substrate pairs. Specifically, we used the 15-mer thrombin-binding aptamer TBA1 of sequence 5'-GGTTGGTGTGGTTGG-3' and the 29-mer TBA2 of sequence 5'-AGTCCGTGGTAGGGCAG-GTTGGGGTACT-3' to recognize, respectively, the exosite I and II of thrombin (Fig. 1B). The elongation of the aptamers with single-stranded stretches (light and dark blue strands in Fig. 1A) provides the link to the DNA origami surface (brown in Fig. 1A). Two types of DNA nanostructures have been designed: a monolayer frame (45) (indicated as “rect”; Fig. 1C) and a bilayer cubic shape (indicated as “box”; Fig. 1E) (46). Both structures display a ca. 20 nm-by-20 nm inner cavity, modified with one or two single-stranded DNA (ssDNA) handles that are complementary to the TBA elongations and are positioned at the opposite sides of the DNA void at a linear distance of about 5 nm (fig. S1). In this way, only one thrombin molecule can be encapsulated in the cavity of each aptamer-modified DNA chamber, as demonstrated by atomic force microscopy (AFM) and transmission electron microscopy (TEM) imaging (Fig. 1, D and F to I, and figs. S2 and S3). Effective binding of TBAs to their target epitopes on the protein surface depends on the correct folding of the aptamer motifs into G-quadruplex structures (Fig. 1B). Using FRET-labeled TBA sequences, we proved the correct formation of the aptamer motifs under the experimental conditions used (fig. S4), as well as their efficient integration within the origami structure (fig. S5). A fluorescently labeled thrombin was lastly used to confirm the specificity of the binding interaction between the protein and the TBA-modified cages (figs. S6 and S7).

All aptamer-modified DNA structures used in this work are indicated as rect or box followed by an apex number that stands for the type of aptamer linked in the cavity (i.e., 1, 2, or 1/2 for TBA1, TBA2, or, both of them, TBA1/2). The extent of structural flexibility at the aptamer/DNA origami interface is instead denoted by a “flex” or “rig” subscript, resulting in five distinct constructs ( $\text{rect}^1_{\text{flex}}$ ,  $\text{rect}^2_{\text{flex}}$ ,  $\text{rect}^{1/2}_{\text{flex}}$ ,  $\text{rect}^{1/2}_{\text{rig}}$ , and  $\text{box}^{1/2}_{\text{rig}}$ ). In both the flex and rig versions, the aptamers are embedded into the cavity of the DNA cage through a duplex (fig. S8). However, whereas in the flexible version, the presence of a nick and/or a single unpaired base at the origami/aptamer interface allows for a certain degree of rotational freedom, in the rigid analog, the aptamers are directly linked to the DNA origami structure through elongation of one of its staple strands and adopt a fixed orientation with respect to the inner walls of the cage. Several controls were also prepared to estimate the geometric and electrostatic contributions given by the DNA origami cages. A premelted rectangular origami structure that bears both aptamers

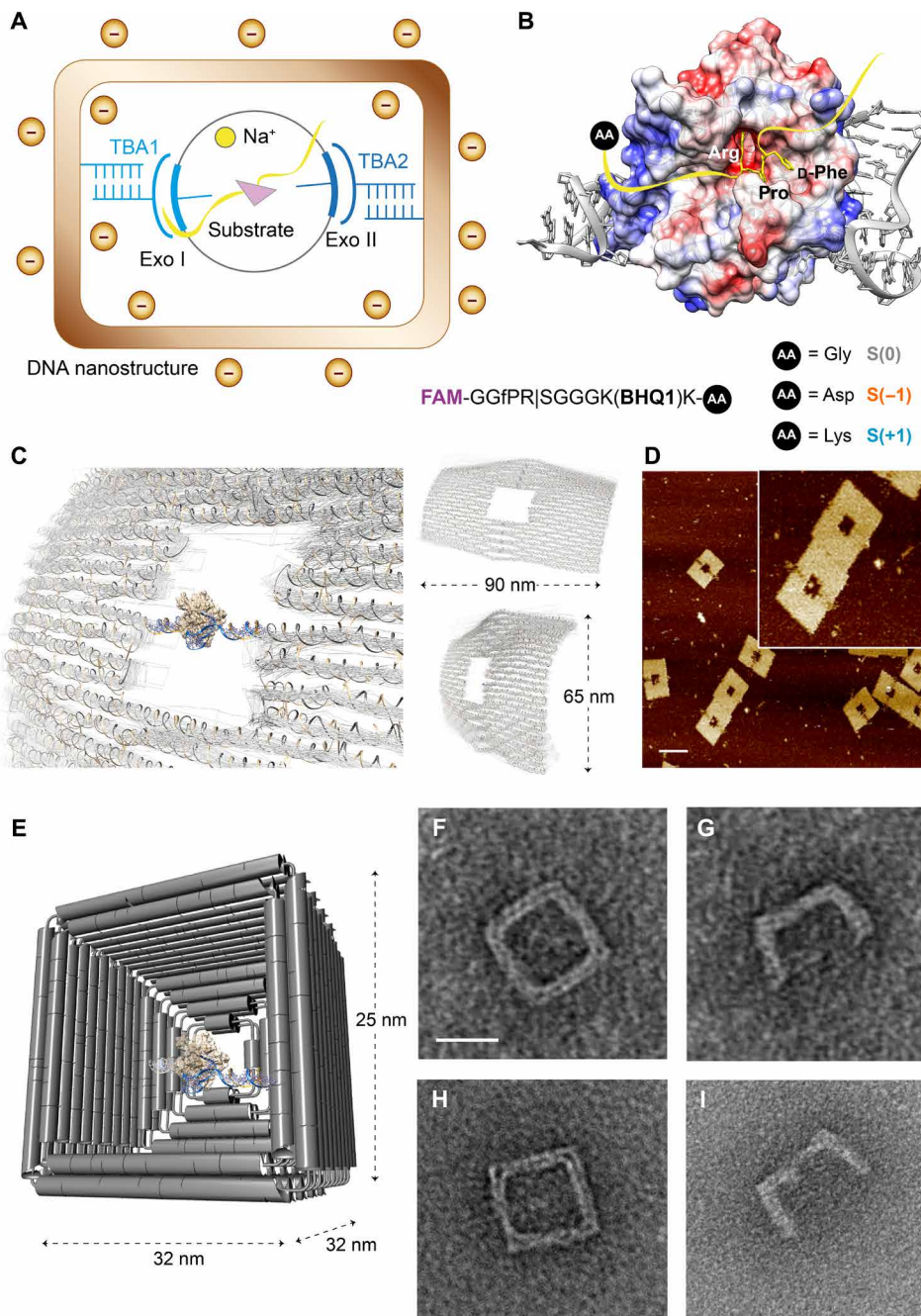


**Fig. 1. The DNA origami thrombin system.** (A) Schematic representation of the DNA-enzyme complex used in our study: A single copy of human  $\alpha$ -thrombin is confined within a DNA origami nanostructure through thrombin-binding aptamers (TBA1 and TBA2) that specifically recognize the exosite I and II of the protein (light and dark blue segments). Peptide cleavage after Arg residue occurs in the deep catalytic pocket (triangular shape). (B) Molecular model showing the interaction of thrombin with the TBAs (gray; Protein Data Bank: 4DIH and 4I7Y). The peptide substrate is schematically represented by a segment (yellow) that spans the protein cleft among the two epitopes. The protein surface is colored according to the charge of the exposed amino acid residues (red to blue means negative to positive charge, respectively). (C) Molecular model of thrombin trapped within the cavity of a TBA-modified rectangular DNA origami (front and side views are also shown). (D) AFM characterization of the rectangular DNA frame in complex with thrombin. Scale bar, 100 nm. (E) Thrombin trapped within the TBA-modified box structure and raw TEM images of the empty (F and G) and thrombin-loaded DNA chamber (H and I) in front and side views. Scale bar, 25 nm.

( $\text{rect}^{1/2}_{\text{melt}}$ ) was used to test the role played by the structural integrity of the DNA shape on the rate of the enzymatic reaction. On the other hand, the effect of unspecific electrostatic interactions between the thrombin and the densely charged DNA origami surfaces

was quantified using DNA structures that lack the inner ligands (rect and box). Last, an equimolar mixture of short ssDNA and a phosphate solution of identical ionic strength (phosph) allowed us to determine whether the spatial density of negative charges around

the protein might be of relevance (all constructs used in this work are schematically illustrated in Fig. 2A).

### Effect of DNA on the thrombin-catalyzed hydrolysis of S(0)

In all our kinetic assays, 1.2 nM thrombin was incubated in a reaction buffer [typically TEMg 1× (20 mM tris, 2 mM EDTA and 12.5 mM MgCl<sub>2</sub> [pH 7.6])] for 1 hour at 37°C, either in the absence or presence of 1 nM aptamers. The latter were added to the solution either as freely diffusing species or as prepurified DNA-origami-tethered structures. Upon addition of the substrate (from 0 to 25 μM), the proteolytic

activity of the enzyme was monitored as a function of time by measuring the increase in the fluorescence signal resulting from substrate cleavage (Fig. 2D). We verified the long-term stability of the enzyme under the experimental conditions used and its linear response in the initial phase of the reaction to exclude any bias due to protein degradation or aggregation (figs. S9 and S10). All experiments were performed under identical conditions, for a total of 14 distinct proteolytic reactions for each substrate, mediated over at least three replicates (standard curves and exemplary progress curves obtained by the thrombin-catalyzed hydrolysis of each substrate are reported

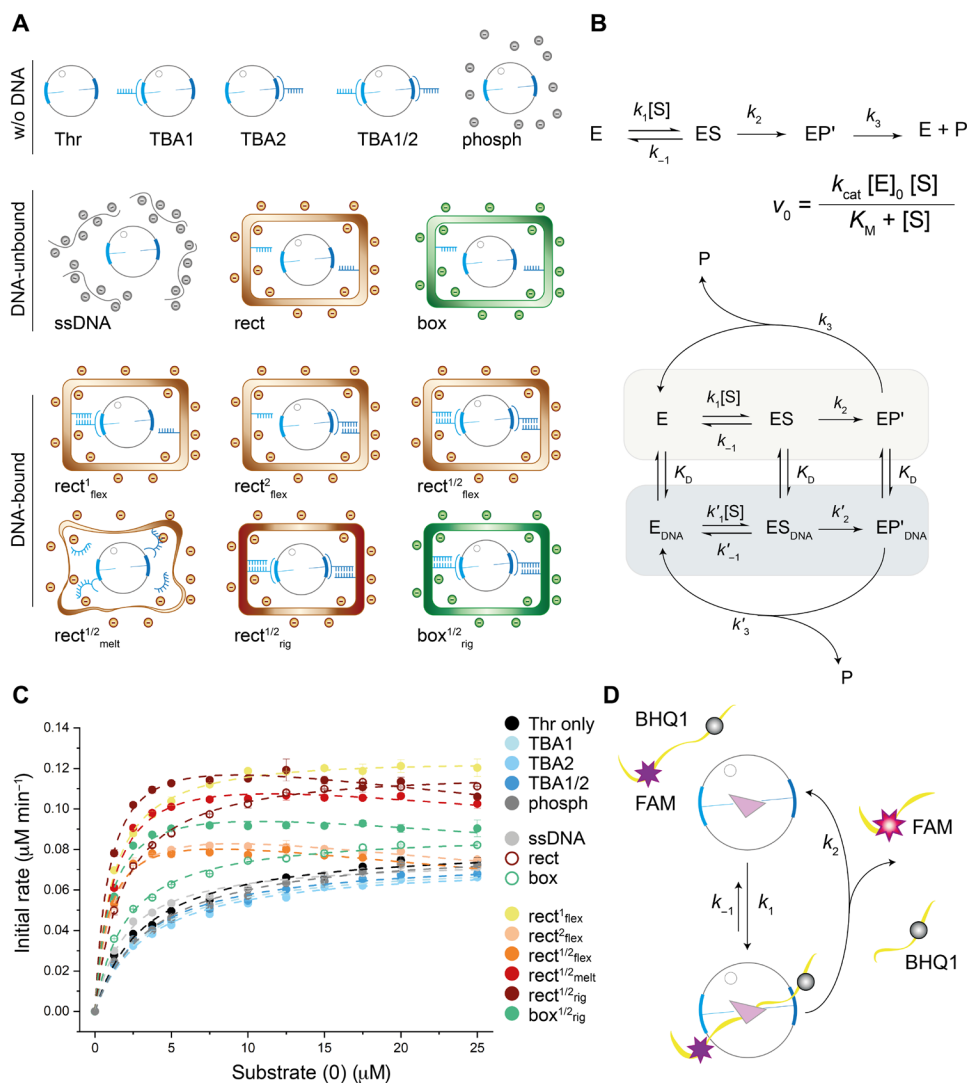


**Fig. 2. Kinetic analysis of thrombin catalyzed hydrolysis of substrate S(0).** (A) All constructs used in this study and their nomenclature. The thrombin-only sample has been compared with samples containing the enzyme in the presence of one (TBA1 and TBA2) or both (TBA1/2) aptamers, either in standard buffer (TEMg 1×) or in a high-ionic strength buffer containing the same concentration of phosphate ions as in the DNA origami samples (phosph). Unspecific electrostatic interactions were evaluated using samples containing the same concentration of DNA, either in the form of single-stranded random chains (ssDNA) or as DNA origami lacking the TBAs (rect and box). The contribution given by scaffolding has been systematically analyzed for various DNA origami constructs. These differ in the number and type of TBAs (rect<sup>1/2</sup><sub>flex</sub>, rect<sup>2</sup><sub>flex</sub>, and rect<sup>1/2</sup><sub>flex</sub>), their rotational freedom within the cavity (rect<sup>1/2</sup><sub>rig</sub>), shape and structural integrity of the cage (box<sup>1/2</sup><sub>rig</sub> and rect<sup>1/2</sup><sub>melt</sub>). (B) The three-step MM mechanism of thrombin, with  $k_{cat}$  and  $K_M$  related in a complex manner to the rate coefficients of the reaction. The presence of different enzyme species in the solution gives rise to a network of interactions, each one characterized by its own MM catalytic cycle. (C) Kinetic profiles (initial rates versus substrate concentration) for the thrombin-catalyzed hydrolysis of substrate S(0) under different conditions. (D) Schematic representation of the catalyzed hydrolysis of the FRET substrate according to a classic two-step MM mechanism.

in figs. S11 to S16). The kinetic profiles (initial rates versus substrate concentration) for  $S(0)$  are reported in Fig. 2C [analog curves for  $S(-1)$  and  $S(+1)$  are reported in fig. S17; background signal control is reported in fig. S18]. The hydrolysis of amide bonds catalyzed by thrombin follows a three-step mechanism, in which the binding ( $k_1$ ) and dissociation ( $k_{-1}$ ) of the substrate are followed by an irreversible acylation ( $k_2$ ) and a final deacylation ( $k_3$ ) step (Fig. 2B, top scheme). Despite the relationship between the Michaelis-Menten (MM) parameters experimentally accessible ( $K_M$  and  $k_{cat}$ ) and the individual rate coefficients here being more complicated than in a classical two-step model, the value of  $k_2$  is typically much lower than  $k_3$ , and for most practical purposes, the reaction can be treated in the usual way, i.e., omitting the last step (text S1). All our velocity curves obey an MM equation (Eq. 1), with DNA origami-tethered enzymes suffering from an apparent inhibition at high substrate concentrations (text S2)

$$v_0 = \frac{k_{cat} [E][S]}{K_M + [S]} \quad (1)$$

Except for  $rect^{1/2}_{flex}$  (yellow curve in Fig. 2C), substrate inhibition occurs in all  $rect$ - and  $box$ -modified structures and is visible by the slight negative slope of the velocity curves for substrate concentrations above  $5 \mu M$  (pink to green curves in Fig. 2C). The kinetic parameters of the reactions were extracted by applying Eq. 1, modified for substrate inhibition when relevant, with  $k_{cat}$  being the turnover number of the enzyme,  $K_M$  the MM constant,  $k_{cat}/K_M$  the specificity constant, and  $K_i$  the dissociation constant of the inhibited enzyme/substrate complex (Fig. 3, text S2, and figs. S19 and S20; numerical values for  $S(0)$  are given in Table 1, and values for  $S(-1)$  and  $S(+1)$  are provided in tables S1 and S2).

A close look at the kinetic parameters obtained for  $S(0)$ , particularly the  $K_M$  (Fig. 3C), permits to distinguish three classes of samples, according to the presence or absence of DNA and its degree of tethering to the enzyme. These classes are identified as “w/o DNA,” “DNA-unbound,” and “DNA-bound.” The first class (w/o DNA) includes all those constructs in which the enzyme is freely diffusing in bulk solution, either in the absence (Thr only, black bar) or presence of one or both aptamers (TBA1, TBA2, or TBA1/2, light to dark blue bars), with the buffer being either the standard one used in all our assays or a sodium phosphate buffer at high ionic strength (phosph, dark gray bar). The common feature of this group, when compared to the other two groups, is the absence of DNA (besides, of course, the aptamers), which results in similar values of  $K_M$  ( $3.4 \pm 0.2 \mu M$ ) and  $k_{cat}$  ( $65 \pm 4 \text{ min}^{-1}$ ). In the DNA-unbound class, the enzyme is still relatively free to move, although being surrounded by a large amount of DNA, a large amount of DNA, either in the form of single-stranded oligonucleotides of random sequence (ssDNA, light gray) or DNA origami structures lacking the aptamers ( $rect$  and  $box$ , unfilled brown and green bars, respectively). This group features a 40% lower  $K_M$  value ( $2.0 \pm 0.1 \mu M$ ) and, on average, a 15% higher  $k_{cat}$  value ( $80 \pm 21 \text{ min}^{-1}$ ) when compared to the w/o DNA class (see also Table 1). Last, the third type of constructs (DNA-bound) is composed of those samples in which the enzyme is mostly immobilized into DNA origami structures. This class is characterized by a further decrease in the  $K_M$  value ( $1.1 \pm 0.2 \mu M$ ) and a further increase in the average value of  $k_{cat}$  ( $100 \pm 14 \text{ min}^{-1}$ ) with respect to the w/o DNA counterpart. Within the DNA-bound group, the number and type of TBAs used to link the enzyme within the DNA cavity do not affect the kinetic parameters of the reaction substantially (see  $rect^{1/2}_{flex}$ ,  $rect^{2/2}_{flex}$ , and

$rect^{1/2}_{flex}$  as yellow, pink, and orange bars, respectively). A similar conclusion can be drawn when considering the structural integrity of the DNA cage, the rigidity of the TBA/DNA connection, or the shape of the cavity (see  $rect^{1/2}_{melt}$ ,  $rect^{1/2}_{rig}$ , and  $box^{1/2}_{rig}$  as red, brown, and green bars, respectively). Essentially, the major feature of this third class of compounds appears to be the tethering of the enzyme to the DNA surface, which, although presumably not quantitative, emphasizes the impact observed in the DNA-unbound enzymes.

Note that, although the concentration of DNA is identical in all samples (1 nM), the total amount of DNA is not, because of the huge difference in the molecular weight of the DNA species used (TBA aptamers versus DNA origami). The microscopic electrostatic environment experienced by the enzyme is therefore extremely different in the three sets of constructs and is presumably the main reason for the observed trend. To resume, the  $K_M$  value of the thrombin/ $S(0)$  reaction decreases to about 60% of its initial value in the presence of large amounts of unbound DNA and reaches only ca. 32% of its initial value when the same number of negative charges is spatially organized around the enzyme in the form of a DNA origami structure. This decrease in  $K_M$  value is accompanied by a moderate increase in the turnover number of the enzyme when compared to the thrombin-only reference, although, here, the trend is less apparent (+16% and +44% for DNA-unbound and DNA-bound constructs, respectively; Fig. 3D).

Assuming a simple MM model, we then applied the transition state theory (47) to relate the kinetic parameters of the reaction to the energy changes experienced by the interacting species along the reaction coordinate (Fig. 4, text S3, and figs. S21 and S22). According to this theory,  $K_M$ ,  $k_{cat}$ , and  $k_{cat}/K_M$  indicate, respectively, the energy barrier between the unreacted  $E + S$  species and the ES complex ( $\Delta G_{ES}$ ), the ES complex and the transition state  $ES^\ddagger$  ( $\Delta G^\ddagger$ ), and, lastly, the unreacted species  $E + S$  and the  $ES^\ddagger$  ( $\Delta G^\ddagger_{TS}$ ). Thus, by calculating the variation in the energy barriers (i.e.,  $\Delta \Delta G_{ES}$ ,  $\Delta \Delta G^\ddagger$ , and  $\Delta \Delta G^\ddagger_{TS}$ ) from the ratio of the corresponding MM parameters in two distinct scenarios (text S3), one can gather useful information on the response of the enzyme to a given perturbation. As this theory relies on the change of energy barriers rather than their absolute values, we assumed that the level corresponding to the initial species ( $E + S$ ) is identical in all situations analyzed and depicted an arbitrary energy diagram for a reaction taken as reference [here, the thrombin/ $S(0)$  reaction]. Two regimes of substrate concentrations are considered,  $[S] < K_M$  and  $[S] > K_M$  (Fig. 4, A and B, respectively), to locate the ES complex either above or below the  $E + S$  level and estimate the impact of those energy changes on the velocity of the reaction.

We restricted our analysis to six representative examples, namely, substrates  $S(0)$ ,  $S(-1)$ , and  $S(+1)$  cleaved either by thrombin only (light lines in Fig. 4) or by a DNA-tethered thrombin ( $box^{1/2}_{rig}$ ; dark lines in Fig. 4). This should help to illustrate the effect of substrate net charge and DNA scaffolding on the energy landscape of the reaction. Our analysis for  $S(0)$  indicates that the surrounding DNA scaffold lowers the energy of the ES complex and, to a slightly larger extent, stabilizes the transition state  $ES^\ddagger$ , too (boxed inset in Fig. 4). The final effect is a decrease of the activation energy barrier ( $\Delta \Delta G^\ddagger = -0.18 \text{ kcal mol}^{-1}$ ), although the reactive ES complex is more stable ( $\Delta \Delta G_{ES} = 0.72 \text{ kcal mol}^{-1}$ ). As  $\Delta G^\ddagger_{TS}$  becomes much smaller in the presence of DNA ( $\Delta \Delta G^\ddagger_{TS} = -0.89 \text{ kcal mol}^{-1}$ ), the value of  $k_{cat}/K_M$  highly increases (fig. S19), accelerating the hydrolysis of  $S(0)$  at low substrate concentrations. Such a favorable DNA-induced effect is instead less pronounced at high concentration regimes, where  $k_{cat}$  is

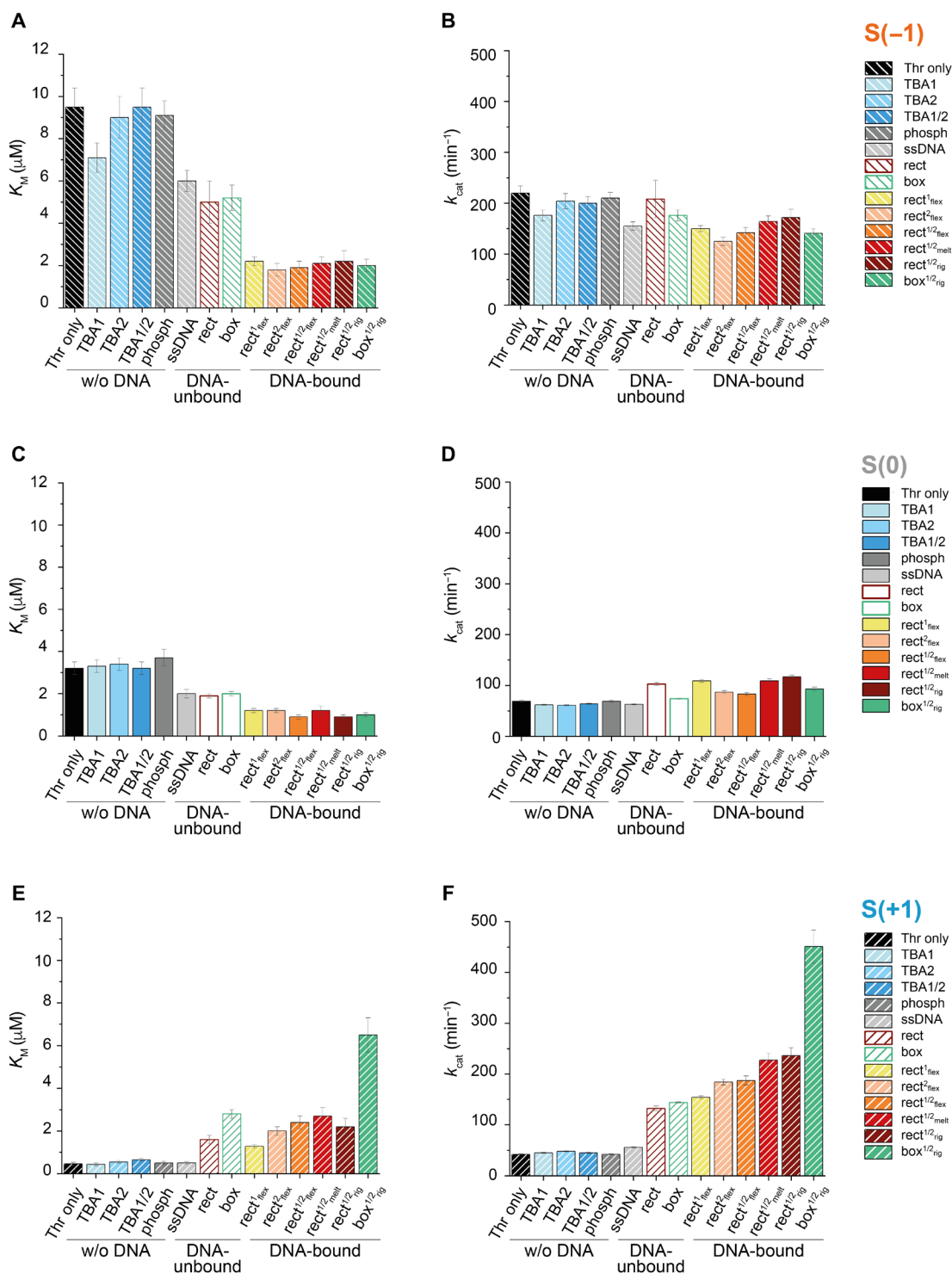


**Fig. 3. Kinetic parameters for the thrombin-catalyzed hydrolysis of the three substrates.** Analysis of the initial velocity curves led to extraction of the kinetic parameters of the reaction, namely, the MM constant ( $K_M$ ), the turnover number ( $k_{cat}$ ), and, when relevant, the inhibition constant ( $K_i$ ; see Table 1). Kinetic values were obtained for hydrolysis of the peptide substrate S(-1) (A and B), S(0) (C and D), and S(+1) (E and F) in a thrombin-only solution (black bars) or in samples containing an identical amount of thrombin with addition of one or both freely diffusing aptamers (light to dark blue bars), one or both aptamers tethered to a flexible (yellow to orange bars), premelted (red), or rigid DNA origami rectangular (brown) or box-like (green) cage. Control origami structures lacking the aptamers (red and green unfilled bars) were also analyzed and solutions containing an identical amount of DNA in single-stranded form (light gray) or phosphate ions (dark gray).

**Table 1. Kinetic parameters for the thrombin-catalyzed hydrolysis of substrate S(0).** Analysis of the kinetic profiles (initial velocity versus substrate concentration) was performed using the MM equation corrected for substrate inhibition (when relevant) and led to extraction of the kinetic parameters of the reaction, namely, the catalytic efficiency or turnover number ( $k_{\text{cat}}$ ), the MM constant ( $K_M$ ), the specificity constant ( $k_{\text{cat}}/K_M$ ), and, when relevant, the inhibition constant ( $K_i$ ). Reported values are the result of at least three replicates.

	Thr/S(0)	$k_{\text{cat}}$ ( $\text{min}^{-1}$ )	$K_M$ ( $\mu\text{M}$ )	$k_{\text{cat}}/K_M$ ( $\text{min}^{-1} \mu\text{M}^{-1}$ )	$K_i$ ( $\mu\text{M}$ )
<b>Thrombin only</b>	–	69 ± 2	3.2 ± 0.3	21 ± 2	–
	TBA1	62 ± 1	3.3 ± 0.3	19 ± 2	–
<b>w/o DNA</b>	TBA2	61 ± 1	3.4 ± 0.3	18 ± 2	–
	TBA1/2	64 ± 1	3.2 ± 0.3	20 ± 2	–
	phosph	69 ± 2	3.7 ± 0.4	18 ± 2	–
	ssDNA	63 ± 1	2.0 ± 0.2	31 ± 3	–
<b>DNA-unbound</b>	rect	103 ± 3	1.9 ± 0.1	55 ± 4	–
	box	74 ± 1	2.0 ± 0.1	37 ± 2	–
	rect <sup>1</sup> <sub>flex</sub>	109 ± 3	1.2 ± 0.1	93 ± 8	–
	rect <sup>2</sup> <sub>flex</sub>	87 ± 3	1.2 ± 0.1	75 ± 9	70 ± 13
<b>DNA-bound</b>	rect <sup>1/2</sup> <sub>flex</sub>	83 ± 3	0.9 ± 0.1	87 ± 12	68 ± 13
	rect <sup>1/2</sup> <sub>melt</sub>	109 ± 4	1.2 ± 0.2	88 ± 12	106 ± 28
	rect <sup>1/2</sup> <sub>rig</sub>	117 ± 3	0.9 ± 0.1	124 ± 13	90 ± 14
	box <sup>1/2</sup> <sub>rig</sub>	93 ± 4	1.0 ± 0.1	89 ± 13	110 ± 31

dominant. The perfect match of these predictions with our experimental observations (Fig. 2C) confirms the suitability of this approach for interpretation of the kinetic data and helps to rationalize the outcomes under a unifying picture.

### Effect of substrate net charge on thrombin kinetics

Next, we performed identical enzymatic assays with S(–1) and S(+1) substrates (Fig. 3, A, B, E, and F; representative progress curves are reported in figs. S13 to S16). As described above, these peptides differ only in the C-terminal residue, namely, an Asp in S(–1) and a Lys in S(+1). This leads, respectively, to a negative and positive net charge of the peptides at neutral pH. The C-terminal region of natural thrombin substrates is known to establish critical electrostatic interactions with the positively charged exosite I on the surface of the protein. The pattern of these interactions and their role in reorienting nearby hydrophobic contacts are thought to be mainly responsible for the high specificity of substrate recognition and thrombin allosteric regulation (31, 39, 40). We therefore expect that these substrates, despite being identical in the portion that binds the active site of thrombin, will show different kinetic signatures. This is what we observed for thrombin-only samples and all analog constructs belonging to the first class (see w/o DNA in Fig. 3, A, C, and E). Compared to S(0), the hydrolysis of substrate S(–1) in the absence of DNA nanostructures exhibits more than a threefold increase in both  $K_M$  (ca. 9  $\mu\text{M}$ ) and  $k_{\text{cat}}$  (ca. 200  $\text{min}^{-1}$ ) values, whereas the corresponding values for substrate S(+1) are definitively lower (ca. 0.5  $\mu\text{M}$  and 45  $\text{min}^{-1}$ , respectively; tables S1 and S2). These data essentially indicate that the interactions between the C-terminal region of the peptides and the exosite I affect the MM parameters in a charge-dependent fashion. Notably, our substrates do not interfere with the binding of the aptamers to the exosite I of thrombin (fig. S23). Again, application of the transition state model helps to interpret this phenomenon in energetic terms (Fig. 4, see bright lines of different colors;

see also fig. S21 and text S3). Specifically, in the absence of DNA, addition of a negative charge to the substrate, i.e., replacing substrate S(0) with S(–1), weakly destabilizes the ES complex, leaving the transition state almost unchanged. On the contrary, addition of a positive charge, i.e., replacing substrate S(0) with S(+1), has an opposite outcome, i.e., it stabilizes both the ES complex and the transition state, with the former being more stabilized than the latter. This clarifies the opposed kinetic signatures of these substrates and explains why, in the absence of DNA, S(–1) is a better substrate than S(0), particularly at high concentrations (where the velocity is mostly affected by  $k_{\text{cat}}$ , i.e.,  $\Delta G^\ddagger$ ), while the reverse behavior is displayed by S(+1). A close look at the effect of substrate net charge on the energy levels of the DNA-confined reaction is also very instructive (Fig. 4, see dark lines of different colors; see also fig. S22). When substituting S(0) with S(–1), the same trend observed in the absence of DNA appears, and thus, similar conclusions can be applied. S(+1) behaves instead in a completely different fashion: Here, the addition of the positive charge in the presence of the surrounding DNA environment largely destabilizes the ES complex, leaving the transition state almost untouched. This translates into a notable increase in  $K_M$  and  $k_{\text{cat}}$ , with  $k_{\text{cat}}/K_M$  being barely affected. This condition is particularly favorable and results into the maximal reaction rate observed at all substrate concentration regimes (up to ca. 0.30  $\mu\text{M} \text{min}^{-1}$ ; fig. S17B). Two main conclusions can be drawn from this analysis: (i) The destabilization of the enzyme-substrate complex, which is critical to improve the catalytic performance of the enzyme, goes along with the addition of negative charges to the substrate (cfr. gray/black lines with orange/red lines in Fig. 4), and (ii) the unfavorable contribution given by the positively charged substrate is largely compensated by a surrounding DNA microenvironment, resulting in the inversion of the catalytic performance of S(+1) when cleaved by a DNA-tethered thrombin (cfr. gray/black lines with cyan/blue lines in Fig. 4). Multiple reasons can be responsible for these phenomena,

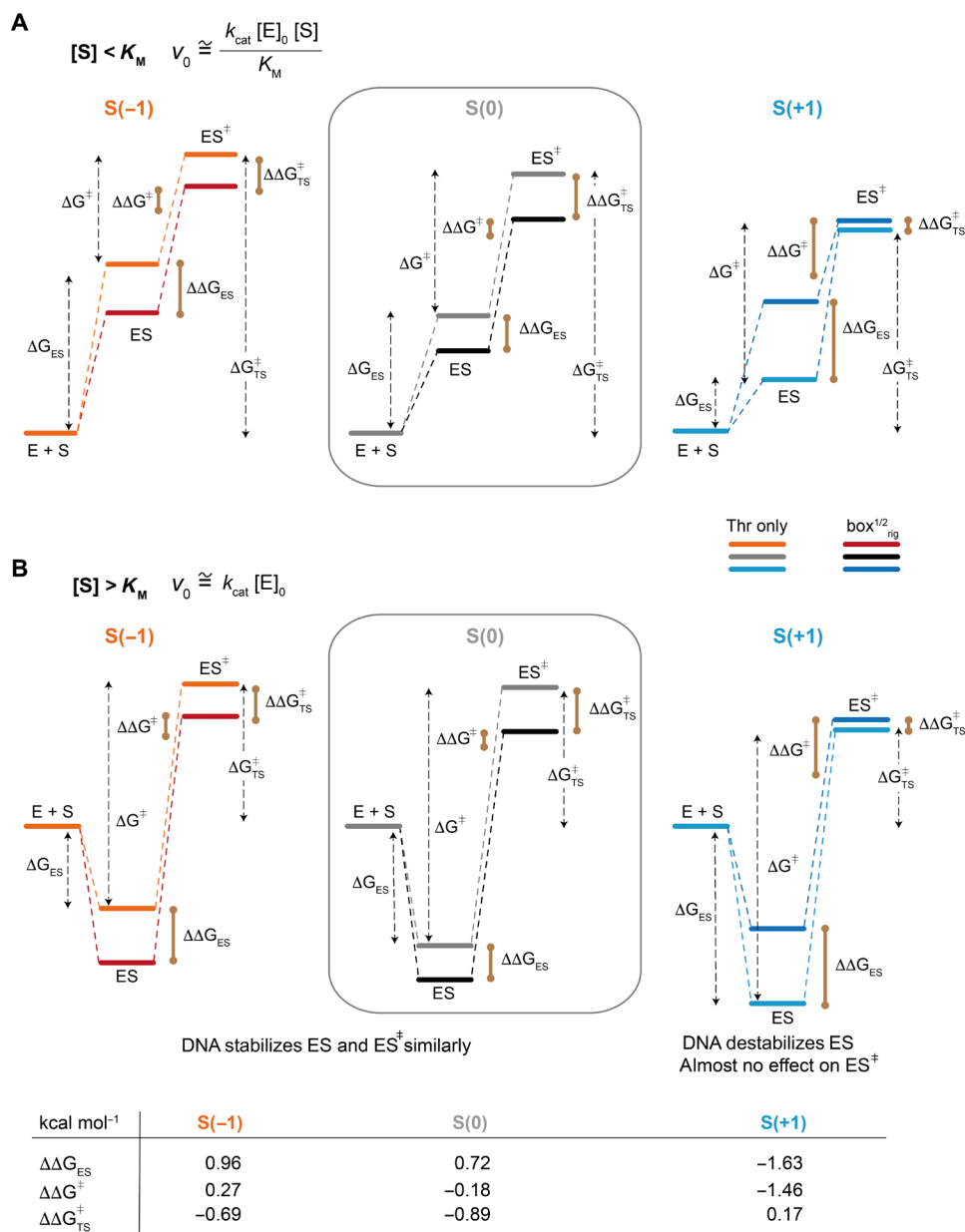


**Fig. 4. Representative energy diagrams for the reaction of S(-1), S(0), and S(+1) with thrombin only and with a DNA-tethered thrombin ( $\text{box}^{1/2}_{\text{rig}}$ ).** Assuming a simple MM mechanism, the transition state theory is applied to estimate the changes in the energy barriers of two distinct reactions, namely, from the unreacted E + S species to the ES complex ( $\Delta\Delta G_{\text{ES}}$ ), from ES to the transition state ES<sup>‡</sup> ( $\Delta\Delta G^{\ddagger}$ ), and from E + S to ES<sup>‡</sup> ( $\Delta\Delta G_{\text{TS}}^{\ddagger}$ ). Two regimes of substrate concentrations are considered ( $[S] < K_M$  and  $[S] > K_M$ , in (A) and (B), respectively) to estimate the impact of those changes on the velocity of the reaction. This approach is applied to compare the variation in the energy landscape of a given substrate hydrolysis when catalyzed by thrombin only (light lanes) or a DNA-tethered thrombin ( $\text{box}^{1/2}_{\text{rig}}$ ; dark lines) and can be used to compare the hydrolysis of different substrates by the same thrombin construct (cfr. orange, gray, and blue lines). The reaction of S(0) with thrombin only is taken as a reference, and its energy diagram is arbitrarily drawn (black inset). The diagrams for all other substrates and reactions are depicted to scale and are therefore fully comparable (numerical values of the calculated changes in energy barriers due to the surrounding DNA scaffold are reported in the table, with positive and negative values indicating, respectively, an increase or a decrease in the energy barrier considered). In our energy diagrams, we assume that the level corresponding to the initial species (E + S) is identical in all situations analyzed, as here, only relative energies rather than absolute values are relevant. For details of the analysis, see text S3 and figs. S21 and S22.

and only structural studies can attempt to give a precise description of the system. Nevertheless, we can deduce that the net charge of the substrate plays a fundamental role in establishing interaction patterns, both with the protein and the DNA scaffold, that are critical for the efficient onset of the enzymatic reaction.

To gain more insights into the enzyme-substrate interactions, we performed Gaussian accelerated MD (GaMD) simulations of our protein/substrate systems (Fig. 5, A to C, top). Under our experimental conditions, thrombin features a deep cleft that includes the catalytic pocket (48). We built three model systems using as template the

crystal structure of the dPhe-Pro-Arg chloromethylketone inhibitor bound to the protein (49). This structure contains the P1-P3 portion of the peptides properly oriented at the catalytic site of thrombin. Our simulations allowed us to explore how the charge at the C terminus of the substrates influences the orientation of the peptides with respect to the exosite I. The large number of positive charges at the exosite I (six Lys and three Arg residues) can determine the observed affinity ranking among the substrates S(-1), S(+1), and S(0) due to dominant electrostatic interactions in this region of the protein (31). Peptide S(+1) exhibits three Lys residues at the C terminus, which, on the basis of our simulations, should be close to the exosite I. The repulsion between these moieties is most likely the reason for the lower affinity of this peptide. Representative binding modes extracted from the main conformational clusters of the simulations (fig. S24) show that, due to that repulsion, S(+1) does not establish close contacts with the exosite I.

On the contrary, the negative charge at the C terminus of the S(-1) peptide is expected to lead to a behavior opposite to that of S(+1). The GaMD simulations show that the C-terminal Asp of S(-1) interacts favorably with positively charged residues in the exosite I and its vicinity (i.e., Lys<sup>60F</sup> and Arg<sup>35</sup> and, to a less extent, Arg<sup>73</sup>; fig. S25). To gain a better understanding of the space covered by the C-terminal residues of the peptides during the whole trajectories, we calculated the density maps of the C-terminal Asp and Lys residues in the S(+1) and S(-1) peptides, respectively (Fig. 5, A to C, bottom). These densities can be interpreted as the regions of highest probability of finding the C-terminal residue of the peptides when forming the complex with thrombin. The results indicate that the density of the C-terminal Asp residue in S(-1) overlaps with the exosite I region (Fig. 5A), while the space covered by the C-terminal Lys residue in the S(+1) peptide is more focused on regions of the protein that do not involve the exosite I (Fig. 5C). Last, our GaMD simulations indicate that S(0) shows a pattern of electrostatic interactions with the exosite I that is similar to that exhibited by the S(-1) peptide (Fig. 5B). This can be explained by the presence of the C-terminal Gly that does not hinder the interaction between the negatively charged carboxylate group of the peptide and the positively charged residues in the exosite I and its vicinity (mainly with Arg<sup>35</sup> and Arg<sup>73</sup>; fig. S26).

Together, the analysis of our biomolecular simulations essentially shows that the charge at the C-terminal position of the peptide can greatly influence the dynamics of the substrate toward the exosite I. Negative or neutral charges at this position preserve favorable electrostatic interactions with the exosite I, thus probably triggering enzyme activation through binding of the substrate to this regulatory region of the protein. On the contrary, the presence of a positive charge in the same position of the substrate is sufficient to disrupt the pattern of favorable electrostatic interactions at the exosite I, down-regulating enzyme activation. In this sense, the extreme plasticity of thrombin and its sensitivity to even tiny changes in the pattern of interactions around its surface are ideal conditions to reveal the impact of DNA in the allosteric regulation of the enzyme.

### The combined role of substrate net charge and DNA scaffolding on thrombin kinetics

Together, our observations highlight the key role played by the electrostatic interactions at the thrombin/substrate interface and how these interactions can be affected by a surrounding DNA microenvironment. To better disentangle the role of DNA in the three-component

system, it is illustrative to report the kinetic parameters as three-dimensional (3D) plots (Fig. 6, A and B). To this end, the relative values of  $K_M$  and  $k_{cat}$  with respect to the reference sample ( $z$  axis) were plotted in dependence on two variables, namely, the extent of DNA/enzyme electrostatic interactions ( $x$  axis) and the substrate net charge ( $y$  axis). Figure 6 (A and B) shows the 3D plots for two sets of representative DNA/enzyme systems. The first set comprises the TBA1/2, rect, and rect<sup>1/2</sup><sub>rig</sub> samples (light-colored bars), whereas the second set includes the TBA1/2, box, and box<sup>1/2</sup><sub>rig</sub> samples (dark-colored bars). The reference element in both sets is a solution of thrombin in the presence of both aptamers (TBA1/2) under freely diffusive conditions. Comparison of the kinetic parameters within each triad provides information on the change in the catalytic performance of thrombin at increasing levels of DNA/enzyme interactions ( $x$  axis: indicated as w/o DNA, DNA-unbound, and DNA-bound). The impact of the net charge of the substrate on the kinetic parameters of the reaction becomes evident by comparing the values obtained from the hydrolysis of different substrates in the same DNA/enzyme setting [ $y$  axis: S(-1), S(0), and S(+1), indicated respectively by orange, gray, and blue bars]. Last, the different behavior exhibited by the two triads reveals the role played by the particular geometry of the DNA cage on the catalytic activity of the trapped enzyme (rectangular frame versus box-like shape, i.e., light versus dark bars of the same color).

The trend of the 3D plot along the  $x$  axis indicates that the extent of thrombin confinement within the DNA walls has a stabilizing effect on the enzyme/substrate complex (i.e., the  $K_M$  value decreases), however, only when the substrate in question is the S(-1) or the S(0) (Fig. 6A, inset, orange and gray bars). In energetic terms, this corresponds to a  $\Delta\Delta G_{ES}$  value of ca. 0.90 kcal mol<sup>-1</sup> for both the rect<sup>1/2</sup><sub>rig</sub> and box<sup>1/2</sup><sub>rig</sub> samples. The presence of S(+1) results instead in a large destabilization of the ternary complex (up to a 14-fold increase in  $K_M$  value), particularly when the enzyme is embedded into a deep DNA cavity, such as the one displayed by the box structure ( $\Delta\Delta G_{ES} = -1.63$  kcal mol<sup>-1</sup>; Fig. 6A, blue bars). The turnover numbers follow a similar trend with almost a 30% reduction of  $k_{cat}$  value in the presence of S(-1) and a 10-fold increase in the presence of S(+1), with S(0) showing intermediate values (Fig. 6B). The analysis of the 3D plot along the  $y$  axis reveals that, whereas the kinetics of the reaction is weakly influenced by the substrate net charge in the presence of DNA aptamers only (Fig. 6, A and B, lane w/o DNA), this is instead not true in the presence of DNA origami structures (DNA-unbound and DNA-bound lanes). Here, the differences between the substrates become more apparent with the largest kinetic effects exhibited when the enzyme is tethered inside a DNA box cavity (blue bars in Fig. 6, A and B). An interesting aspect of these ternary complexes therefore emerges: When favorable DNA/substrate interactions compensate unfavorable binding patterns at the enzyme/substrate interface, a weak allosteric effector such as the S(+1) can turn into a strong one, and this effect is proportional to the extent of enzyme confinement within the DNA cage (Fig. 6C).

To further investigate this phenomenon, we built a coarse-grained (CG) model of the flexible monolayer rectangular frame with one thrombin unit attached to the aptamers (resembling our rect<sup>1/2</sup><sub>flex</sub> structure) and solvated it with a CG model of water. The solvated DNA origami model comprised more than 3 million CG particles. The initial structure displayed a mostly planar configuration with the DNA origami, thrombin, and aptamers laying roughly on the same plane (Fig. 5D). This structure was used as the starting point for the

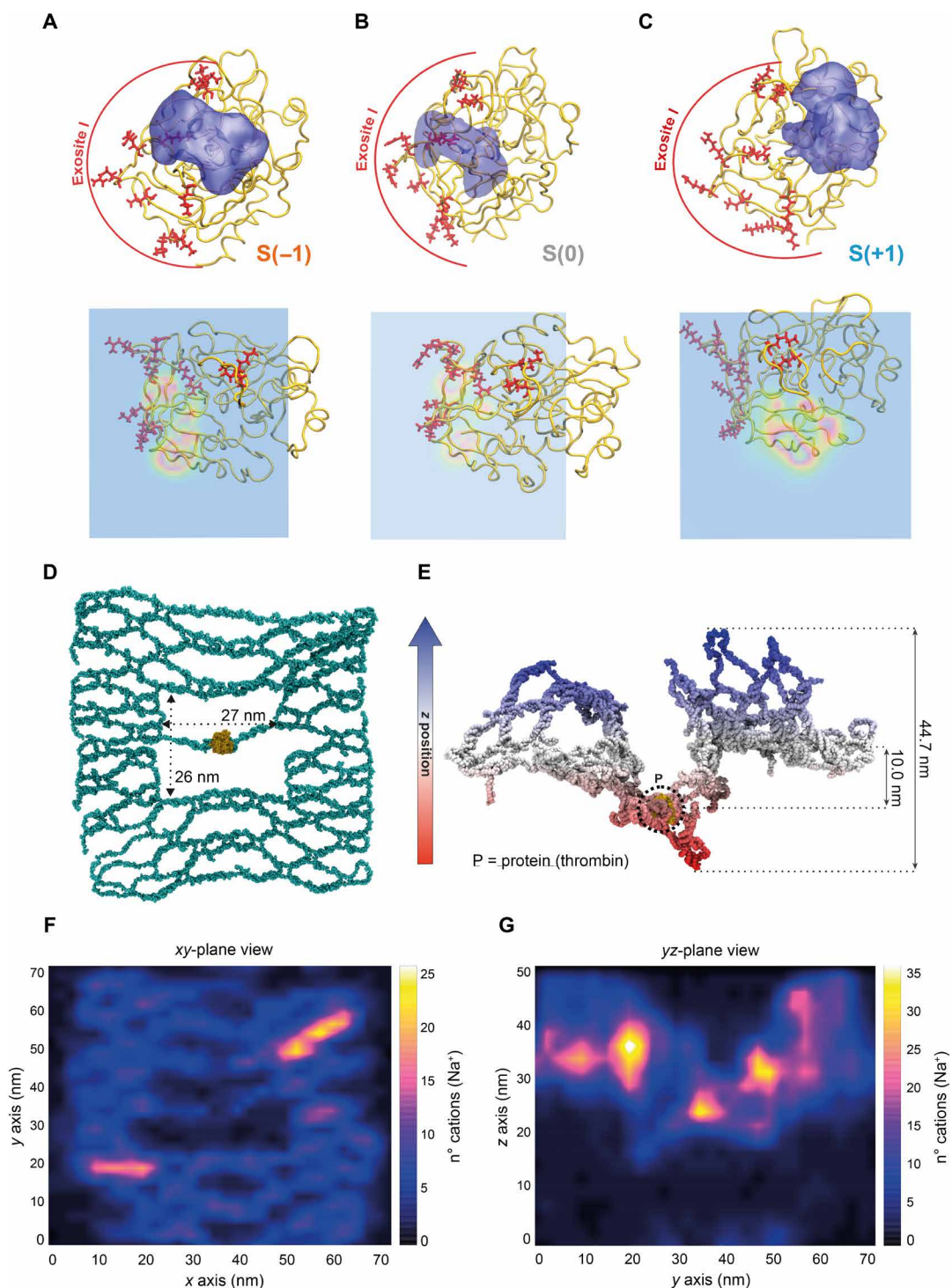


**Fig. 5. MD simulation studies.** The regions with the highest probability of finding the C-terminal residue of peptides S(-1), S(0), and S(+1) (A to C) during the GaMD simulations are shown as mass densities at isovalues of 0.01. Bottom panels show horizontal slices along the xz plane with an offset value of 0.6 (representing the position of the slice with respect to the y axis in a scale from 0 to 1). The brighter areas represent larger values of the density, while blue areas correspond to zero or very low densities. (D) Initial structure of the model consisting of the DNA origami, the aptamers, and thrombin in a nearly planar configuration. Thrombin (in yellow) is located inside the DNA cavity. The DNA strands are shown in green. (E) Structure of the DNA-thrombin system after 120-ns MD simulations. Thrombin is located close to the bottom of a depression formed by the flexible DNA scaffold. The protein (P), shown in yellow, is encircled for easier visualization. The DNA origami is colored on the basis of the position of its particles along the z axis. Red regions correspond to particles located deeper in the DNA origami, while blue regions represent particles with high values of their z coordinates. The white regions are those located close to the plane defined by the initial structure shown in (D). The depth of the depression where the protein is located is about 10 nm. The distribution of sodium ions in solution is viewed as a 2D projection on the xy (F) and yz (G) planes. Density maps are represented in a pseudo-color scale, with higher concentrations of sodium ions corresponding to brighter colors.

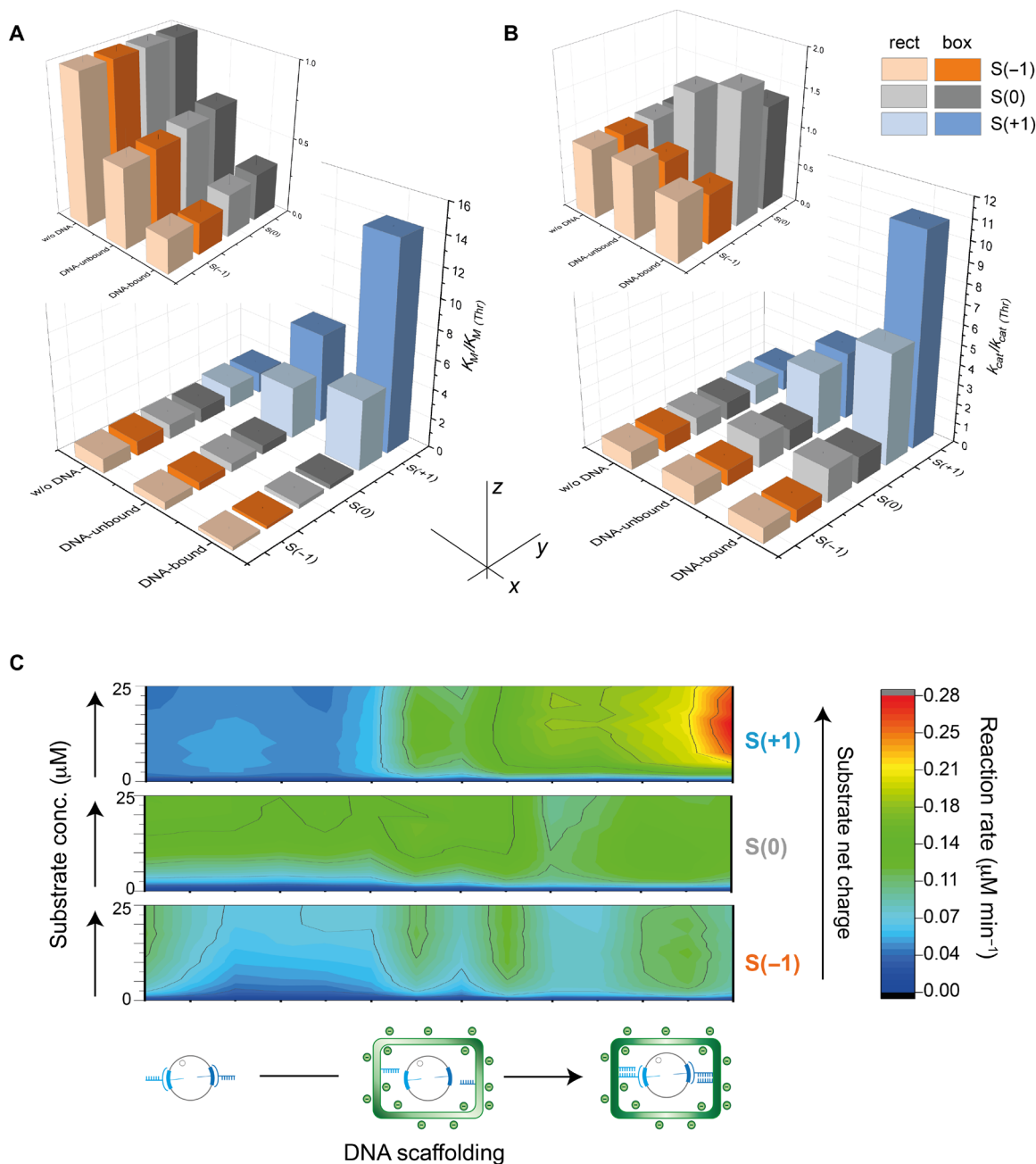


**Fig. 6. Effect of DNA on the kinetics of thrombin-catalyzed hydrolysis.** The relative values of  $K_M$  (**A**) and  $k_{cat}$  (**B**) with respect to the thrombin-only reference sample [ $K_{M(Thr)}$  and  $k_{cat(Thr)}$ ] are plotted as a function of DNA scaffolding (w/o DNA, DNA-unbound, and DNA-bound) and substrate net charge [from  $S(-1)$  to  $S(0)$  to  $S(+1)$ , respectively, in orange, gray, and blue] and for two sets of representative samples. These are the TBA1/2, rect, and  $rect^{1/2}_{rig}$  (light-colored bars) and the TBA1/2, box, and  $box^{1/2}_{rig}$  (dark-colored bars). (**C**) 2D contour plot illustrating the impact of DNA scaffolding on the velocity of the reaction at different substrate net charges and concentration regimes. The rate of the reaction is represented in pseudocolors as a heatmap (blue to red colors correspond to a 0 to  $0.28 \mu M \text{ min}^{-1}$  scale). The extent of DNA/enzyme tethering is schematically represented by three structures, corresponding, from left to right, to a free, DNA-unbound, and DNA-bound thrombin. Reaction rates are typically low in free-thrombin systems, with  $S(+1)$  exhibiting the lowest performance. DNA scaffolding of the enzyme results in the enhancement of the reaction rates for all substrates, particularly at moderate and high concentrations, with  $S(+1)$  becoming now the best performing substrate.

MD simulations (three independent replicas of 120, 140, and 400 ns, respectively). The results show that the DNA monolayer is very flexible and adopts a wave-like shape with hollow regions devoid of DNA of about 20 nm by 20 nm in size (Fig. 5E). In all simulations,

the protein is located in one of these depressions, the depth and shape of which vary as a consequence of the large flexibility of the structure. Notably, although the entire structure is rather flexible, the aptamers remain bound to thrombin at both exosites during the

entire simulation time. This observation highlights the stability of the aptamers' binding and their suitability to trap the enzyme at the desired position of the DNA cage. It is reasonable to presume that, since the DNA origami is a highly charged polymeric structure, the strongly anisotropic electrostatic field generated by the DNA surface should affect the spatial distribution of positively charged particles in its direct vicinity. We used the cations present in the solution as probes to verify this hypothesis. As predicted, sodium ion density maps [see  $z$  axis in Fig. 5 (F and G)] indicate that the cations are mostly concentrated nearby the origami.

Accordingly, S(+1) molecules are expected to show a higher tendency to accumulate at the DNA origami surface when compared to the other substrates, with consequent substrate inhibition already at moderate substrate concentrations (50). This type of binding mode is often observed in proteolytic enzymes when more than one substrate molecule partially binds to different portions of the active site, such that none of them can be effectively cleaved, leading to an apparent inhibition (text S2). In full agreement with our hypothesis, nonproductive binding is mostly relevant for S(+1) in the presence of aptamer-modified DNA origami structures, leading to minimal values of  $K_i$  in the box-like structures (Table 1, tables S1 and S2, and fig. S20). This idea is further confirmed by the fact that ca. 10  $\mu\text{M}$  concentration of S(+1) is already sufficient to induce the formation of aggregates, whereas no aggregation is visible for the other substrates up to 25  $\mu\text{M}$  concentration (figs. S27 to S30). The initial phase of the reaction is, however, free from aggregation events, enabling to use this time interval for extrapolation of the kinetic parameters of substrate hydrolysis (fig. S31). The time-course cleavage of S(+1) is also characterized by the appearance of hysteresis above a substrate threshold concentration (around 5 to 7.5  $\mu\text{M}$ ) and only in the presence of DNA origami structures (figs. S32 and S33). Hysteresis is indicative of a delay in the time response of the enzyme and leads to a sigmoidal, rather than hyperbolic, shape of the dose-response curve (51, 52). This behavior is evident also at low substrate levels when the variable parameter is the DNA origami concentration, confirming once again the strength of the electrostatic interactions between S(+1) and the DNA-thrombin complex (fig. S34).

To further test the effect of charges on the kinetics of the reaction, we analyzed the thrombin-catalyzed hydrolysis of S(+1) at different pH values (fig. S35). The data show that lower pH values do affect the rate of the enzymatic reaction, however, in a negative fashion, thereby excluding that the lower value of pH around the DNA-scaffolded thrombin may be responsible for the enhanced catalysis observed and that, more likely, additional ions might be involved in interactions with critical amino acid residues on the protein surface (53). This is further supported by comparing the rates obtained for all substrates at different concentrations of magnesium ions, either in the absence or presence of an aptamer-modified DNA origami structure (fig. S36). The results show that, in general, the amidase activity of thrombin is largely affected by the concentration of ions and that favorable DNA/substrate electrostatic interactions may transform a poorly efficient hydrolysis into a sixfold faster reaction [cfr. S(-1), S(0), and S(+1) at 6 mM magnesium ions].

### The effect of multiple enzyme species on thrombin catalysis

The binding of thrombin to our DNA origami structures is mediated by noncovalent interactions with G4-aptamers; therefore, formation of the DNA-enzyme complexes relies on an equilibrium reaction and is typically not quantitative. This, of course, poses questions

on the quantification of the effect attributed to DNA scaffolding, as one would expect this to be proportional to the fraction of DNA-bound species. Binding yields, as estimated by single-particle imaging, varied from ca. 5%, in the box DNA origami structure, to a maximum of about 44%, in the rectangular frame structure (figs. S2 and S3). Although these values may be impaired by sample preparation and surface imaging conditions, the fraction of DNA-enzyme complexes experimentally observed matches very well with the expected amount calculated for a  $K_D$  value in the nanomolar range (text S4) (35). Our kinetic data thus refer to a mixture of free and DNA-bound enzyme species in solution and let us suppose that the true effect of DNA scaffolding is largely underestimated. Further binding assays using the switchSENSE technology indicate that thrombin retains its binding specificity also in the presence of a large excess of ssDNA (figs. S37 and S38 and table S3). Upscaling sample preparation in the attempt to isolate the DNA-bound species at high concentrations (>200 nM) and quantify their binding affinity by spectroscopic methods led, in our hands, to undesired aggregation phenomena. A successful purification of the target species would, however, lead to the initial issue again, as the use of noncovalently bound DNA-enzyme complexes at the low concentrations typically applied in kinetic assays would result into the reestablishment of an equilibrium mixture.

A method is therefore needed to analyze networks of enzymatic reactions, where different enzyme species coexist in a pseudo-equilibrium regime: Each species is capable to perform the catalytic cycle, however, with distinct rate coefficients (Fig. 2B). A major contribution to this field comes from Di Cera and coauthors (54) in their formulation of the so-called kinetic linkage scheme of thrombin in the presence of an allosteric effector. The main idea behind this theoretical approach is to describe the steady-state rate of the reaction in a rigorous mathematical fashion, considering all possible kinetic fluxes that link the interacting species (text S5). The expression of the initial velocity is a complicated function of all rate coefficients involved in the network and, despite not being of any real practical use, is instructive to appreciate the kinetic features of the system under a given condition. Inspired by this work, we simulated a network of reactions, composed of two catalytic cycles, one associated to the free enzyme (E) and the other to the DNA-bound enzyme ( $E_{\text{DNA}}$ ), linked by a DNA-enzyme interaction with a given  $K_D$  value (fig. S39 and text S5). For simplicity, unspecific DNA-protein interactions and conformational transitions of thrombin are not considered in our model. We performed various kinetic simulations using values reported in the literature (53, 55) for the rate coefficients of thrombin under diffusive conditions similar to those used in our experiments and tested the influence of the  $E_{\text{DNA}}$  pathway on the steady-state rate of the reaction for different values of  $K_D$  (from 0.1 nM to 1  $\mu\text{M}$ ; fig. S40). The results show that the reaction velocity is dominated by the faster enzyme even if this is the least-abundant species. This effect can be easily understood, considering that the linkage described in our simulations is of kinetic (and not thermodynamic) origin and indicates the rate of the reaction at the steady-state regime, i.e., in the initial phase of the enzymatic reaction. On the bases of these data, we lastly simulated a possible set of conditions that lead to the velocity curves observed for S(0), S(-1), and S(+1), either in the absence or presence of DNA origami, and evidenced that a higher catalytic performance of the  $E_{\text{DNA}}$  species may dominate the steady-state rate of the reaction even if present at low concentrations and that a substrate-dependent partition of fluxes

among the two pathways may be responsible for the compliant kinetic behavior of thrombin observed (fig. S41).

## DISCUSSION

The general picture emerging from all our data can be summarized as follows: The kinetic cycle catalyzed by thrombin is affected by two structural parameters of the system, i.e., the C-terminal residue of the substrate and the presence of a DNA nanostructure. Whereas the former affects the catalytic reaction via an allosterically regulated site of the protein, the latter instead tunes the kinetic behavior of the enzyme mainly through electrostatic interactions with both the enzyme and the substrate. In this way, specific patterns of interactions at the enzyme/substrate interface can be drastically altered when the enzyme is spatially confined into a DNA nanostructure. The steady-state rate of the reaction often increases in the presence of DNA, independently of the substrate used. However, the mechanism that leads to such an enhancement and its extent is largely dependent on the net charge of the substrate and its concentration, with the neutral and negatively charged substrates exhibiting fast cleavage rates mainly through stabilization of the transition state, while the positively charged substrate takes advantage of a DNA-induced destabilization of the enzyme-substrate complex. Thus, both binding and chemical activation energies seem to be affected by the presence of a surrounding DNA environment, and probably only structural studies can try to give a detailed explanation of this phenomenon. Notoriously, electrostatic charges play a fundamental role in the enzymatic activity of thrombin and are important in the regulation of several other serine proteases, such as chymotrypsin and subtilisin (47). Therefore, it is reasonable to think that the presence of a dense layer of negative charges around the protein may influence the ionic environment nearby the enzyme surface, altering the pK of critical ionizable residues and triggering ion-dependent mechanisms of allosteric regulation, essentially creating alternative kinetic routes for substrate cleavage. These DNA-driven fluxes may dominate the steady-state rate of the reaction even in the presence of minimal amounts of DNA-scaffolded enzymes, provided that their intrinsic kinetics is sufficiently faster. This can result in the inversion of the catalytic signature of ionizable substrates with respect to their performance under free diffusive conditions, with the slowest substrate becoming the fastest and the fastest substrate becoming instead the slowest. In this sense, DNA nanostructures can amplify the catalytic differences among substrates with distinct net charge and may be used to modulate networks of catalytic reactions in a programmable yet general fashion. The identification and quantification of the electrostatic contributions of DNA nanostructures become thus important for a deeper understanding of the catalytic features of DNA-scaffolded enzymes and may eventually inspire new tools for the rational programming of enzymatic catalysis.

## MATERIALS AND METHODS

### DNA design and sample preparation

DNA sequences, including FAM- and 5-carboxytetramethylrhodamine (TAMRA)-modified aptamers (TBA1: GGTTGGTGTGGTTGG and TBA2: AGTCCGTGGTAGGGCAGGTTGGGGTGACT), were purchased from Sigma-Aldrich with high-performance liquid chromatography-grade purity (Merck, Germany). The peptide substrates [FAM-GGfPR|SGGGK(BHQ-1)K-Aaa-OH with Aaa = G, K,

or D] were purchased from Intavis Peptide Services GmbH (Germany). Human  $\alpha$ -thrombin (2000 National Institutes of Health U/mg) was purchased by Cayman Chemical (#13188, Germany). DNA origami structures were designed with caDNAno (<https://cadnano.org>) and assembled using a 1:6 molar ratio between the M13mp18 ssDNA scaffold (40 nM) and each of the staple strands, in TEMg 1× buffer [20 mM tris, 2 mM EDTA, and 12.5 mM MgCl<sub>2</sub> (pH 7.6)]. Thermal annealing was performed by decreasing the temperature from 80° to 20°C at −1°C/min on a Thermocycler Mastercycler nexus gradient (Eppendorf), upon an initial denaturation at 80°C for 5 min. DNA origami samples were purified by polyethylene glycol precipitation. Their concentration was determined by quantitative polymerase chain reaction (qPCR) or spectrophotometrically (see below) and adjusted to the final desired value in the assay buffer before use for the enzymatic studies.

### Agarose gel electrophoresis

Analysis of samples by gel imaging was performed by using a 1% agarose (Lonza) gel in TBEMg 1× buffer [40 mM tris base, 20 mM boric acid, 2 mM EDTA and 12.5 mM Mg acetate (pH 8.0)], at 80 V for 2 hours at 4°C. The gel was scanned with a Typhoon FLA9000 (GE Healthcare Life Sciences) at different wavelengths and lastly stained with ethidium bromide.

### Quantification of DNA nanostructures

DNA nanostructures were quantified using either the DS-11 Spectrophotometer FX+ (DeNovix) or by means of qRT-PCR. In the latter case, a specific TaqMan probe targeting the m13mp18 backbone was used, as well as a specific forward and reverse primer for amplification (Thermo Fisher Scientific, #4331348). A calibration curve was obtained by using a dilution series of the m13mp18 plasmid. The dilution series was fitted using a linear function with which the sample concentration was calculated. The instrument used for the PCR experiments was a CFX96 real-time system. The software used was the CFX Manager 3.0 (Bio-Rad).

### Enzymatic activity assays

Kinetic data of thrombin-catalyzed reactions were obtained by diluting a stock solution of human  $\alpha$ -thrombin (Cayman Chemicals, #13188; MW 38 kDa) to a final concentration of 1.2 nM in TEMg 1× buffer. Depending on the sample, DNA origamis or free TBAs were added with a final concentration of 1 nM. ssDNA samples were added with 2 nM to compensate for the lack of scaffold. Phosphate samples contained 14.5  $\mu$ M sodium phosphate (VWR Chemicals) to simulate the negative charges. Fifty microliters of the mixture was pipetted to each well of a 96-well plate (Corning, #3991) and incubated at 37°C for 1 hour. Last, 50  $\mu$ l of the respective substrate solution (0 to 25  $\mu$ M final concentration, diluted in TEMg 1× buffer; Intavis) was added to each well. Plates were transferred to a multiplate reader (TECAN Spark10M), and fluorescence was measured immediately every minute for 80 min in total. Each sample was measured as a triplicate. The kinetic parameters of the enzymatic reaction were extracted using the OriginPro software.

### AFM imaging

The sample was deposited on freshly cleaved mica surface (Plano GmbH) and adsorbed for 3 min at room temperature. After washing with ddH<sub>2</sub>O, the sample was dried under gentle argon flow and scanned in ScanAsyst Mode using a MultiMode microscope (Bruker)

equipped with a Nanoscope V controller, using cantilevers with sharpened pyramidal tips (ScanAsyst-Air tips, Bruker). Several AFM images were acquired from different locations of the mica surface to ensure reproducibility of the results. AFM yield was estimated from a total of ca. 7000 structures obtained from several independent preparations. All images were analyzed by using the NanoScope Analysis 1.5 software.

### TEM imaging

For the TEM analysis of origami structures, 400-mesh carbon-coated copper grids (Quantifoil) were glow-discharged and coated with 5  $\mu$ l of the sample. After incubation for 2 min, excess liquid was blotted off, and the sample was stained with 1% uranyl formate before drying. The instrument used was a JEOL JEM 1400 Plus.

### MD simulations

The DNA origami structure was built as a reduced model of the experimental design. Upon coarse-graining and solvating the system, the total number of particles was  $\sim$ 3 million. The SIRAH 2.0 force field (56) and the GROMACS 2019.2 software (57) were used for the simulations. Harmonic restraints were used for the G-quadruplex structures of the aptamers, since no CG sodium ion fits into the ion binding pocket of the aptamer. MD simulations of the DNA origami/thrombin complexes were performed in CG water. To ensure consistency, three independent replicas of 120, 140, and 400 ns were performed. SIRAH is designed to reproduce the structural stability of DNA and other biomolecular systems (56). The SIRAH force field is parametrized using CG monovalent counter ions representing  $\text{Na}^+$  or  $\text{Cl}^-$  and their water shell (up to ca. 11 molecules); thus, the simulations were set up using these particles instead of the  $\text{Mg}^{2+}$  ions present in the experiments. The initial coordinates of our protein/substrate model were extracted from the crystal structure of the dPhe-Pro-Arg fragment in complex with thrombin [Protein Data Bank (PDB) ID: 1PPB] (49). The peptide/thrombin systems were solvated in explicit TIP3P water molecules (58), and after equilibration, they were subjected to three independent production runs of GaMD simulations (59) of 100 ns each. The simulations were performed using a time step of 2 fs, at a constant pressure of 1 bar and a temperature of 300 K. The first 10 ns of production MD were discarded for the analysis of the trajectories. PME (Particle mesh Ewald) (60) was used for the treatment of long-range electrostatic interactions. The simulations were performed using NAMD 2.13 (61, 62) and the CHARMM36m force field (63, 64). For the fluorophores, the parameters were obtained from the Swissparam server (65) and the Match server (66), except for the diazo region, for which parameters from the literature were used (67). For the visualization and analysis of the simulations, the program VMD 1.9.3 (68) was used. A cutoff of 5.0  $\text{\AA}$  for the root mean square deviation was used for the clustering analysis.

### Thrombin/TBA binding assays

Thrombin (Haematologic Technologies Inc., Essex Junction, VT, USA) binding to TBA1, TBA2, or both was measured with switchSENSE technology. All experiments were performed on a heliX<sup>+</sup> instrument (Dynamic Biosensors GmbH, Martinsried, DE) on standard Adapter switchSENSE chips (ADP-48-2-0) using the static measurement mode. The experimental workflow was set up using the proprietary heliOS software (v1.3.1). Scrambled sequences (TBA<sub>sc1</sub> and TBA<sub>sc2</sub>) were used as control sequences. Experiments were performed by mixing 500 nM aptamers (or control sequences) with 400 nM of the

relevant adapter strand harboring a red or green dye for 1 hour in TE40 (10 mM tris-HCl, 40 mM NaCl, 0.05% Tween 20, 50  $\mu$ M EDTA, and 50  $\mu$ M EGTA). Premixed solutions were then hybridized to the corresponding anchor strand covalently attached to the surface of the chip. Kinetic measurements were performed in TE140 running buffer with a flow rate of 500  $\mu$ l/min at 25°C using 100 nM thrombin with or without increasing concentrations (from 0 to 1  $\mu$ M) of a 48-mer DNA oligo that is not complementary to any sequence of the assay (5'-ATC AGC GTT CGA TGC TTC CGA CTA ATC AGC CAT ATC AGC TTA CGA CTA-3'). Excitation and emission bands for the red and green dyes were 600 to 630/650 to 685 nm and 485 to 515/525 to 575 nm, respectively. Surface regenerations were performed at the beginning of each measurement set. The fluorescence traces were analyzed with the heliOS software (v1.3.1, Dynamic Biosensors GmbH, DE) by fitting association and dissociation curves with a single-exponential fit model. Values reported represent the association ( $k_a$ ) and dissociation ( $k_d$ ) rate coefficient; the equilibrium dissociation constant  $K_D$  was measured as  $K_D = k_d/k_a$ . All DNA sequences are listed in the Supplementary Materials.

### Kinetic simulations

All kinetic simulations were performed using the DynaFit program available free of charge at <http://biokin.com>. A network of  $3 \times 2$  enzyme species was created using the following parameters:  $[\text{E}]_0 = 1.2$  nM,  $[\text{DNA}]_0 = 1$  nM. For the free-thrombin (E) pathway, the following rate coefficients were used to simulate, respectively, the association and dissociation of the enzyme ( $k_1 = 6000$   $\text{min}^{-1} \mu\text{M}^{-1}$ ;  $k_{-1} = 16,000$   $\text{min}^{-1}$ ), its irreversible acylation ( $k_2 = 100$   $\text{min}^{-1}$ ), and irreversible deacylation step ( $k_3 = 500$   $\text{min}^{-1}$ ). Values of rate coefficients were taken from the literature for thrombin-catalyzed substrate degradation of peptide substrates in buffer conditions similar to those used in our experiments (53, 55). The reaction of the  $\text{E}_{\text{DNA}}$  species with the substrate ( $\text{E}_{\text{DNA}}$  pathway) was simulated using three sets of rate coefficients for the analog catalytic steps: namely,  $k_4$ ,  $k_{-4}$ ,  $k_5$ , and  $k_6$  that are equal (set 1), 100-fold (set 2), or 0.01-fold (set 3) the values of  $k_1$ ,  $k_{-1}$ ,  $k_2$ , and  $k_3$  (E pathway), respectively. The two kinetic cycles are assumed to be in a pseudo-equilibrium regime that links the enzyme species of the E route to the corresponding enzyme species of the  $\text{E}_{\text{DNA}}$  route according to the same  $K_D$  value. Four different  $K_D$  values were tested: 0.1, 1, and 10 nM, and 1.0  $\mu$ M, obtained from on-rates  $k_7 = k_8 = k_9 = 10,000$   $\text{min}^{-1} \mu\text{M}^{-1}$  and, respectively, off-rates  $k_{-7} = k_{-9} = 1, 10, 100$ , and  $10,000$   $\text{min}^{-1}$ . The value of  $k_{-8} = (k_1 k_8 k_{-4} k_{-7}) / (k_{-1} k_7 k_4)$  is used to satisfy the thermodynamic cycle. Rate coefficients were modified as in fig. S41 to simulate a thrombin-catalyzed hydrolysis of S(0) and S(+1). The effect of DNA was simulated imposing a  $K_D = 1$  nM and rate coefficients for the  $\text{E}_{\text{DNA}}$  pathway, correspondingly, 3-fold and 10-fold the values of the rate coefficients in the E pathway of S(0) and S(+1).

### SUPPLEMENTARY MATERIALS

Supplementary material for this article is available at <https://science.org/doi/10.1126/sciadv.abk0425>

[View/request a protocol for this paper from Bio-protocol.](#)

### REFERENCES AND NOTES

1. K. S. Rabe, J. Müller, M. Skoupi, C. M. Niemeyer, Cascades in compartments: En route to machine-assisted biotechnology. *Angew. Chem. Int. Ed.* **56**, 13574–13589 (2017).
2. C. Teller, I. Willner, Organizing protein-DNA hybrids as nanostructures with programmed functionalities. *Trends Biotechnol.* **28**, 619–628 (2010).

3. W. Engelen, B. M. Janssen, M. Merckx, DNA-based control of protein activity. *Chem. Commun.* **52**, 3598–3610 (2016).
4. J. B. Trads, T. Topping, K. V. Gothelf, Site-selective conjugation of native proteins with DNA. *Acc. Chem. Res.* **50**, 1367–1374 (2017).
5. Y. Hu, C. M. Niemeyer, From DNA nanotechnology to material systems engineering. *Adv. Mater.* **31**, 1806294 (2019).
6. A. Jaekel, P. Stegemann, B. Sacca, Manipulating enzymes properties with DNA nanostructures. *Molecules* **24**, (2019).
7. K. Zhou, J. Dong, Y. Zhou, J. Dong, M. Wang, Q. Wang, Toward precise manipulation of DNA–protein hybrid nanoarchitectures. *Small* **15**, 1804044 (2019).
8. J. Fu, Z. Wang, X. H. Liang, S. W. Oh, E. St. Iago-McRae, T. Zhang, DNA-scaffolded proximity assembly and confinement of multienzyme reactions. *Top. Curr. Chem.* **378**, 38 (2020).
9. X. Lv, S. Cui, Y. Gu, J. Li, G. du, L. Liu, Enzyme assembly for compartmentalized metabolic flux control. *Metabolites* **10**, (2020).
10. D. Zhao, Y. Kong, S. Zhao, H. Xing, Engineering functional DNA-protein conjugates for biosensing, biomedical, and nanoassembly applications. *Top. Curr. Chem.* **378**, 41 (2020).
11. C. M. Niemeyer, J. Koehler, C. Wuerdemann, DNA-directed assembly of bienzymic complexes from in vivo biotinylated NAD(P)H:FMN oxidoreductase and luciferase. *ChemBiochem* **3**, 242–245 (2002).
12. V. V. Demidov, N. V. Dokholyan, C. Witte-Hoffmann, P. Chalasani, H. W. Yiu, F. Ding, Y. Yu, C. R. Cantor, N. E. Broude, Fast complementation of split fluorescent protein triggered by DNA hybridization. *Proc. Natl. Acad. Sci. U.S.A.* **103**, 2052–2056 (2006).
13. L. Fruk, J. Muller, C. M. Niemeyer, Kinetic analysis of semisynthetic peroxidase enzymes containing a covalent DNA-heme adduct as the cofactor. *Chemistry* **12**, 7448–7457 (2006).
14. M. Glettenberg, C. M. Niemeyer, Tuning of peroxidase activity by covalently tethered DNA oligonucleotides. *Bioconjug. Chem.* **20**, 969–975 (2009).
15. Y. H. Lao, K. Peck, L. C. Chen, Enhancement of aptamer microarray sensitivity through spacer optimization and avidity effect. *Anal. Chem.* **81**, 1747–1754 (2009).
16. Y. N. Gao, C. C. Roberts, J. Zhu, J.-L. Lin, C. A. Chang, I. Wheeldon, Tuning enzyme kinetics through designed intermolecular interactions far from the active site. *ACS Catal.* **5**, 2149–2153 (2015).
17. J. Fu, Y. R. Yang, S. Dhakal, Z. Zhao, M. Liu, T. Zhang, N. G. Walter, H. Yan, Assembly of multienzyme complexes on DNA nanostructures. *Nat. Protoc.* **11**, 2243–2273 (2016).
18. G. Ke, M. Liu, S. Jiang, X. Qi, Y. R. Yang, S. Wootten, F. Zhang, Z. Zhu, Y. Liu, C. J. Yang, H. Yan, Directional regulation of enzyme pathways through the control of substrate channeling on a DNA origami scaffold. *Angew. Chem. Int. Ed. Engl.* **55**, 7483–7486 (2016).
19. Z. Zhao, J. Fu, S. Dhakal, A. Johnson-Buck, M. Liu, T. Zhang, N. W. Woodbury, Y. Liu, N. G. Walter, H. Yan, Nanocaged enzymes with enhanced catalytic activity and increased stability against protease digestion. *Nat. Commun.* **7**, (2016).
20. G. Grossi, M. D. E. Jepsen, J. Kjems, E. S. Andersen, Control of enzyme reactions by a reconfigurable DNA nanovault. *Nat. Commun.* **8**, 992 (2017).
21. W. P. Klein, R. P. Thomsen, K. B. Turner, S. A. Walper, J. Vranish, J. Kjems, M. G. Ancona, I. L. Medintz, Enhanced catalysis from multienzyme cascades assembled on a DNA origami triangle. *ACS Nano* **13**, 13677–13689 (2019).
22. J. Muller, C. M. Niemeyer, DNA-directed assembly of artificial multienzyme complexes. *Biochem. Biophys. Res. Commun.* **377**, 62–67 (2008).
23. O. I. Wilner, S. Shimron, Y. Weizmann, Z. G. Wang, I. Willner, Self-assembly of enzymes on DNA scaffolds: En route to biocatalytic cascades and the synthesis of metallic nanowires. *Nano Lett.* **9**, 2040–2043 (2009).
24. O. I. Wilner, Y. Weizmann, R. Gill, O. Lioubashevski, R. Freeman, I. Willner, Enzyme cascades activated on topologically programmed DNA scaffolds. *Nat. Nanotechnol.* **4**, 249–254 (2009).
25. J. Fu, M. Liu, Y. Liu, N. W. Woodbury, H. Yan, Interenzyme substrate diffusion for an enzyme cascade organized on spatially addressable DNA nanostructures. *J. Am. Chem. Soc.* **134**, 5516–5519 (2012).
26. V. Linko, M. Eerikainen, M. A. Kostiainen, A modular DNA origami-based enzyme cascade nanoreactor. *Chem. Commun.* **51**, 5351–5354 (2015).
27. O. Idan, H. Hess, Origins of activity enhancement in enzyme cascades on scaffolds. *ACS Nano* **7**, 8658–8665 (2013).
28. Y. Zhang, S. Tsitkov, H. Hess, Proximity does not contribute to activity enhancement in the glucose oxidase-horseradish peroxidase cascade. *Nat. Commun.* **7**, 13982 (2016).
29. J. A. Huntington, Molecular recognition mechanisms of thrombin. *J. Thromb. Haemost.* **3**, 1861–1872 (2005).
30. W. Bode, D. Turk, A. Karshikov, The refined 1.9-Å x-ray crystal structure of D-Phe-Pro-Arg chloromethylketone-inhibited human alpha-thrombin: Structure analysis, overall structure, electrostatic properties, detailed active-site geometry, and structure-function relationships. *Protein Sci.* **1**, 426–471 (1992).
31. G. Chahal, M. Thorpe, L. Hellman, The importance of exosite interactions for substrate cleavage by human thrombin. *PLOS ONE* **10**, e0129511 (2015).
32. L. C. Bock, L. C. Griffin, J. A. Latham, E. H. Vermaas, J. J. Toole, Selection of single-stranded DNA molecules that bind and inhibit human thrombin. *Nature* **355**, 564–566 (1992).
33. R. F. Macaya, P. Schultze, F. W. Smith, J. A. Roe, J. Feigon, Thrombin-binding DNA aptamer forms a unimolecular quadruplex structure in solution. *Proc. Natl. Acad. Sci. U.S.A.* **90**, 3745–3749 (1993).
34. K. Padmanabhan, K. P. Padmanabhan, J. D. Ferrara, J. E. Sadler, A. Tulinsky, The structure of alpha-thrombin inhibited by a 15-mer single-stranded DNA aptamer. *J. Biol. Chem.* **268**, 17651–17654 (1993).
35. D. M. Tasset, M. F. Kubik, W. Steiner, Oligonucleotide inhibitors of human thrombin that bind distinct epitopes. *J. Mol. Biol.* **272**, 688–698 (1997).
36. I. Russo Krauss, A. Merlino, C. Giancola, A. Randazzo, L. Mazzarella, F. Sica, Thrombin-aptamer recognition: A revealed ambiguity. *Nucleic Acids Res.* **39**, 7858–7867 (2011).
37. A. Aghebat Rafat, S. Sagredo, M. Thalhammer, F. C. Simmel, Barcoded DNA origami structures for multiplexed optimization and enrichment of DNA-based protein-binding cavities. *Nat. Chem.* **12**, 852–859 (2020).
38. X. Chen, B. Jia, Z. Lu, L. Liao, H. Yu, Z. Li, Aptamer-integrated scaffolds for biologically functional DNA origami structures. *ACS Appl. Mater. Interfaces* **13**, 39711–39718 (2021).
39. J. A. Huntington, Thrombin plasticity. *Biochim. Biophys. Acta Proteins Proteom.* **1824**, 246–252 (2012).
40. E. Di Cera, Thrombin. *Mol. Aspects Med.* **29**, 203–254 (2008).
41. M. Pozsgay, G. Szabó, S. Bajusz, R. Simonsson, R. Gáspár, P. Elődi, Study of the specificity of thrombin with tripeptidyl-p-nitroanilide substrates. *Eur. J. Biochem.* **115**, 491–495 (1981).
42. R. R. Cook, B. J. McRae, J. C. Powers, Kinetics of hydrolysis of peptide thioester derivatives of arginine by human and bovine thrombins. *Arch. Biochem. Biophys.* **234**, 82–88 (1984).
43. D. T. Rijkers, S. J. Wielders, G. I. Tesser, H. C. Hemker, Design and synthesis of thrombin substrates with modified kinetic parameters. *Thromb. Res.* **79**, 491–499 (1995).
44. E. Di Cera, Thrombin: A paradigm for enzymes allosterically activated by monovalent cations. *C. R. Biol.* **327**, 1065–1076 (2004).
45. E. C. Schoneweiss, B. Sacca, The collective behavior of spring-like motifs tethered to a DNA origami nanostructure. *Nanoscale* **9**, 4486–4496 (2017).
46. M. Erkelenz, R. Kosinski, O. Sritharan, H. Giesler, B. Sacca, S. Schlücker, Site-specific facet protection of gold nanoparticles inside a 3D DNA origami box: A tool for molecular plasmonics. *Chem. Commun.* **57**, 3151–3153 (2021).
47. A. Fersht, *Structure and Mechanism in Protein Science* (World Scientific, 2017), in Series in Structural Biology, vol. 9.
48. J. A. Huntington, How Na<sup>+</sup> activates thrombin – a review of the functional and structural data. *Biol. Chem.* **389**, 1025–1035 (2008).
49. W. Bode, I. Mayr, U. Baumann, R. Huber, S. R. Stone, J. Hofsteenge, The refined 1.9 Å crystal structure of human alpha-thrombin: Interaction with D-Phe-Pro-Arg chloromethylketone and significance of the Tyr-Pro-Pro-Trp insertion segment. *EMBO J.* **8**, 3467–3475 (1989).
50. A. Cornish-Bowden, *Fundamentals of Enzyme Kinetics* (Wiley-Blackwell, 2012).
51. C. Frieden, Slow transitions and hysteretic behavior in enzymes. *Annu. Rev. Biochem.* **48**, 471–489 (1979).
52. K. E. Neet, G. R. Ainslie Jr., Hysteretic enzymes. *Methods Enzymol.* **64**, 192–226 (1980).
53. E. Di Cera, R. De Cristofaro, D. J. Albright, J. W. Fenton, Linkage between proton binding and amidase activity in human alpha-thrombin: Effect of ions and temperature. *Biochemistry* **30**, 7913–7924 (1991).
54. E. Di Cera, Q. D. Dang, Y. Ayala, A. Vindigni, Linkage at steady state: Allosteric transitions of thrombin. *Methods Enzymol.* **259**, 127–144 (1995).
55. C. M. Wells, E. Di Cera, Thrombin is a Na<sup>+</sup>-activated enzyme. *Biochemistry* **31**, 11721–11730 (1992).
56. M. R. Machado, E. E. Barrera, F. Klein, M. Sónora, S. Silva, S. Pantano, The SIRAH 2.0 Force Field: Altius, Fortius, Citius. *J. Chem. Theor. Comput.* **15**, 2719–2733 (2019).
57. M. J. Abraham, T. Murtola, R. Schulz, S. Páll, J. C. Smith, B. Hess, E. Lindahl, GROMACS: High performance molecular simulations through multi-level parallelism from laptops to supercomputers. *SoftwareX* **1–2**, 19–25 (2015).
58. W. L. Jorgensen, J. Chandrasekhar, J. D. Madura, R. W. Impey, M. L. Klein, Comparison of simple potential functions for simulating liquid water. *J. Chem. Phys.* **79**, 926–935 (1983).
59. Y. T. Pang, Y. Miao, Y. Wang, J. A. McCammon, Gaussian accelerated molecular dynamics in NAMD. *J. Chem. Theor. Comput.* **13**, 9–19 (2017).
60. T. Darden, D. York, L. Pedersen, Particle mesh Ewald: An N-log(N) method for Ewald sums in large systems. *J. Chem. Phys.* **98**, 10089–10092 (1993).
61. J. C. Phillips, R. Braun, W. Wang, J. Gumbart, E. Tajkhorshid, E. Villa, C. Chipot, R. D. Skeel, L. Kalé, K. Schulten, Scalable molecular dynamics with NAMD. *J. Comput. Chem.* **26**, 1781–1802 (2005).
62. J. C. Phillips, D. J. Hardy, J. D. C. Maia, J. E. Stone, J. V. Ribeiro, R. C. Bernardi, R. Buch, G. Fiorin, J. Héning, W. Jiang, R. McGreevy, M. C. R. Melo, B. K. Radak, R. D. Skeel, A. Singharoy, Y. Wang, B. Roux, A. Aksimentiev, Z. Luthey-Schulten, L. V. Kalé, K. Schulten,

- C. Chipot, E. Tajkhorshid, Scalable molecular dynamics on CPU and GPU architectures with NAMD. *J. Chem. Phys.* **153**, 044130 (2020).
63. K. Vanommeslaeghe, A. D. MacKerell Jr., CHARMM additive and polarizable force fields for biophysics and computer-aided drug design. *Biochim. Biophys. Acta* **1850**, 861–871 (2015).
64. J. Huang, S. Rauscher, G. Nawrocki, T. Ran, M. Feig, B. L. de Groot, H. Grubmüller, A. D. MacKerell Jr., CHARMM36m: An improved force field for folded and intrinsically disordered proteins. *Nat. Methods* **14**, 71–73 (2016).
65. V. Zoete, M. A. Cuendet, A. Grosdidier, O. Michielin, SwissParam: A fast force field generation tool for small organic molecules. *J. Comput. Chem.* **32**, 2359–2368 (2011).
66. J. D. Yesselman, D. J. Price, J. L. Knight, C. L. Brooks III, MATCH: An atom-typing toolset for molecular mechanics force fields. *J. Comput. Chem.* **33**, 189–202 (2012).
67. M. Krol, T. Borowski, I. Roterman, B. Piekarska, B. Stopa, J. Rybarska, L. Konieczny, Force-field parametrization and molecular dynamics simulations of Congo red. *J. Comput. Aided Mol. Des.* **18**, 41–53 (2004).
68. W. Humphrey, A. Dalke, K. Schulten, VMD: Visual molecular dynamics. *J. Mol. Graph.* **14**, 33–38 (1996).

**Acknowledgments:** We are grateful to E. Di Cera (Saint Louis, MO) and group for the insightful discussions and guidance. We thank M. Hasenberg and B. Walkenfort (IMCES, Essen) for providing access to the TEM facility. **Funding:** This work was supported by the German

Research Foundation (grant SA 1952/3-1 to B.S. and CRC 1093 projects A6 to B.S., A8 to E.S.-G., and A9 to S.S.). E.S.-G. acknowledges funding from the DFG (Projektnummer: 436586093) and Germany's Excellence Strategy (EXC 2033, grant 390677874). E.S.-G. also acknowledges the support of the Boehringer Ingelheim Foundation (Plus-3 Program). **Author contributions:** R.K., J.M.P., E.-C.S., Y.B.R.-B., E.S.-G., and B.S. conceived the experiments. R.K. performed the DNA assembly, kinetic assays, and AFM imaging and analyzed the kinetic data. J.M.P. and Y.B.R.-B. performed the MD simulations and analyzed the modeling data with E.S.-G. K.B.-R. built the initial origami model. I.P. and G.U. performed and analyzed the binding assays with the switchSENSE technology. AFM-based binding assays were performed by E.-C.S. M.E. and S.S. performed and analyzed the TEM imaging. B.S. and E.S.-G. wrote the manuscript. All authors discussed the results and commented on the manuscript. **Competing interests:** The authors declare that they have no competing interests. **Data and materials availability:** All data needed to evaluate the conclusions in the paper are present in the paper and/or the Supplementary Materials. PDB codes 4DIH and 4I7Y are available free of charge, respectively, at <https://rcsb.org/structure/4DIH> and <https://rcsb.org/structure/4I7Y>.

Submitted 18 June 2021

Accepted 10 November 2021

Published 5 January 2022

10.1126/sciadv.abk0425